Applied Thermal Engineering 190 (2021) 116796

Contents lists available at ScienceDirect

Applied Thermal Engineering

journal homepage: www.elsevier.com/locate/ate

Research paper

Sensitivity of transcritical cycle and turbine design to dopant fraction in CO_2-based working fluids

O.A. Aqel *, M.T. White, M.A. Khader, A.I. Sayma

Department of Mechanical Engineering and Aeronautics, City, University of London, Northampton Square, London EC1V 0HB, UK

ARTICLE INFO

Keywords:
Transcritical Rankine cycle
Axial turbine
Sensitivity analysis
CSP
CO_2-based mixtures
Dry-cooling

ABSTRACT

Supercritical CO_2 (sCO_2) power cycles have gained prominence for their expected excellent performance and compactness. Among their benefits, they may potentially reduce the cost of Concentrated Solar Power (CSP) plants. Because the critical temperature of CO_2 is close to ambient temperatures in areas with good solar irradiation, dry cooling may penalise the efficiency of sCO_2 power cycles in CSP plants. Recent research has investigated doping CO_2 with different materials to increase its critical temperature, enhance its thermodynamic cycle performance, and adapt it to dry cooling in arid climates.

This paper investigates the use of $CO_2/TiCl_4$, CO_2/NOD (an unnamed Non-Organic Dopant), and CO_2/C_6F_6 mixtures as working fluids in a transcritical Rankine cycle implemented in a 100 MWe power plant. Specific focus is given to the effect of dopant type and fraction on optimal cycle operating conditions and on key parameters that influence the expansion process. Thermodynamic modelling of a simple recuperated cycle is employed to identify the optimal turbine pressure ratio and recuperator effectiveness that achieve the highest cycle efficiency for each assumed dopant molar fraction. A turbine design model is then used to define the turbine geometry based on optimal cycle conditions.

It was found that doping CO_2 with any of the three dopants ($TiCl_4$, NOD, or C_6F_6) increases the cycle's thermal efficiency. The greatest increase in efficiency is achieved with $TiCl_4$ (up to 49.5%). The specific work, on the other hand, decreases with $TiCl_4$ and C_6F_6, but increases with NOD. Moreover, unlike the other two dopants, NOD does not alleviate recuperator irreversibility. In terms of turbine design sensitivity, the addition of any of the three dopants increases the pressure ratio, temperature ratio, and expansion ratios across the turbine. The fluid's density at turbine inlet increases with all dopants as well. Conversely, the speed of sound at turbine inlet decreases with all dopants, yet higher Mach numbers are expected in CO_2/C_6F_6 turbines.

1. Introduction

Supercritical CO_2 (sCO_2) power cycles have been investigated for various energy sources such as nuclear, fossil fuels, waste heat and concentrated solar power [1]. Several studies have identified the potential of sCO_2 cycles to outperform traditional steam cycles in concentrated solar power (CSP) plants [2–7], potentially making CSP more competitive with solar photovoltaics (PV). It does so by increasing the power block thermal efficiency while decreasing its complexity and size, thus lowering the capital cost of the plant. However, one of the challenges facing sCO_2 systems for CSP applications persists; the requirement of wet cooling. Water scarcity necessitates the use of dry cooling, which prevents condensing cycles, increases the cycle's compression work, and limits its efficiency. Consequently, more complex cycles may be required to reduce compression work and realise higher efficiencies. Alternatively, doping CO_2 with an additional fluid to produce a CO_2-based mixture could alleviate the limitations of dry cooling by increasing the critical temperature of the working fluid.

Firstly, a distinction must be made between a CO_2 mixture and its dopant. The latter is any chemical additive that is added to CO_2 to produce the former. For instance, a mixture of $CO_2/TiCl_4$ consists of CO_2 as its base fluid and $TiCl_4$ as the dopant. The use of dopants is being explored as means to adapt CO_2 properties to better suit various applications, including CSP. In theory, mixing CO_2 with other fluids may increase or decrease its critical temperature and pressure, depending on the added dopant. Dopants with critical temperatures higher than CO_2 tend to increase the critical temperature of the working fluid, whilst those with lower critical temperatures have the opposite effect. However, this is a general trend that has many exceptions, namely in the presence of zeotropic mixtures such as CO_2-ethane [8].

* Corresponding author.
E-mail address: Omar.Aqel@city.ac.uk (O.A. Aqel).

https://doi.org/10.1016/j.applthermaleng.2021.116796
Received 23 September 2020; Received in revised form 3 February 2021; Accepted 23 February 2021
Available online 1 March 2021

Nomenclature

Acronyms

AAD	Average Absolute Deviation
BIP	Binary Interaction Parameter
CSP	Concentrated Solar Power
EoS	Equation of State
HTM	Heat Transfer Medium
LMTD	Log-Mean Temperature Difference
MITA	Minimum Internal Temperature Approach
NOD	Non-Organic Dopant
PHE	Primary Heat Exchanger
sCO_2	Supercritical Carbon Dioxide
SPT	Solar Power Tower
TES	Thermal Energy Storage
VLE	Vapour–Liquid Equilibrium

Greek Symbols

η	Efficiency (%)
γ	Adiabatic coefficient
Λ	Degree of reaction
ω	Rotational speed (rpm)
ω_s	Specific speed
ϕ	Flow coefficient
ψ	Loading Coefficient

Roman Symbols

b	Blade height (m)
c	Chord length (m)
C_p	Isobaric heat capacity (J K^{-1} kg^{-1})
h	Specific enthalpy (J kg^{-1})
k_{ij}	Binary interaction coefficient
M	Molecular mass (kg^{-1} mol^{-1})
m	Mass (kg)
P	Pressure (Pa)
Q	Heat load (W)
R	Ideal gas constant (J kg^{-1})
r	Pressure ratio
S	Pitch (m)
S_a	Allowable stress (Pa)
S_e	Endurance limit (Pa)
T	Temperature (K)
t	Thickness (m)
T_r	Reduced temperature
W	Work (W)

Subscripts

H	Heat source
L	Heat sink
P	Pump
s	Isentropic
sat	Saturation
t	Turbine

Different dopants have been proposed for different application temperatures. For example, applications for which the heat sink temperatures are well below 31.1 °C may benefit from dopants that lower the working fluid's critical temperature. On the other hand, dopants that increase the critical temperature of the fluid enable condensation to be achieved using dry cooling. This expands the operation of transcritical carbon dioxide (tCO_2) cycles, which compress the fluid in its liquid state and expand it in its supercritical state, into arid environments [9].

The benefit of using CO_2 dopants has been explored in the past. Most recently, Valencia-Chapi et al. [10] quantified the effect of using 12 different CO_2-based mixtures on a recompression cycle coupled with line-focusing CSP plants. They found that mixtures increase cycle thermal efficiency by 3%–4%, depending on the heat sink temperature and the mode of cooling.

Jeong & Jeong [11] investigated CO_2-H_2S and CO_2-cyclohexane mixtures, which have higher critical temperatures than pure CO_2. They concluded that these mixtures will deteriorate simple recuperated cycle efficiency due to the narrowing of the difference between the heat source and sink temperatures, but will have favourable effects on a recompression cycle since both compressors will operate near the critical point and benefit from real gas effects. The phenomenon of real gas effects in hydrocarbon CO_2 mixture cycles was studied by Invernizzi & Van Der Stelt [12] as well. They noted that the mixtures had lower heat transfer coefficients, which has the adverse effect of increasing the size and cost of the heat exchangers.

Similarly, Xia et al. [13] optimised cycles using different CO_2–organic compounds mixtures and identified certain mixtures that may lead to improved cycle performance. However, hydrocarbon mixtures are not stable enough for temperatures above 400 °C, which is the expected temperature range of CSP [12], hence alternatives are needed.

Two such alternatives were proposed by Manzolini et al. [14]. By blending CO_2 with small fractions of dinitrogen tetroxide (N_2O_4) and titanium tetrachloride ($TiCl_4$), the critical temperature of the working fluid was increased to around 50 °C, which enables an air-cooled condenser to be used in locations with relatively high ambient temperatures (higher than 40 °C). The dopants were chosen due to their thermal stability and their higher critical temperatures compared to CO_2. The mass fraction ratios were set to CO_2-$TiCl_4$ 85%–15% and CO_2-N_2O_4 78% to 22% based on a previous optimisation [15]. Cycle optimisation carried out at high turbine entry temperatures of 550 and 700 °C resulted in cycle efficiencies up to 50%, a reduction of 50% and 20% in specific costs of the power block with respect to conventional steam cycle and sCO_2 power blocks, and a reduction of 11 to 13% of levelized cost of electricity (LCoE) with respect to a conventional steam cycle.

A host of cycle configurations have been studied for CO_2 power plants, as noted by Crespi et al. [16]. Among those studied is the simple recuperated cycle, which consists of a compressor/pump, primary heat exchanger, turbine, recuperator, and cooler. Its appeal comes from its use of recuperation to benefit from high turbine outlet temperatures and improve efficiency whilst maintaining a simple layout, which translates to lower capital costs. With CO_2 as its working fluid, a simple recuperated cycle exhibits significant exergy destruction in the recuperator as a result of the difference in the heat capacity rates between the hot and cold streams. Several other cycle configurations have been devised to reduce recuperator irreversibility. For example, the recompression and partial cooling achieve this by dividing the recuperator into two stages and splitting the flow between them. However, Manzolini et al. [14] have demonstrated that the use of dopants may reduce recuperator irreversibility by reducing the heat capacity rate difference between the hot and cold streams.

The promising results of Manzolini et al. [14] brought forth the EU funded H2020 SCARABEUS project [17]. The project identifies blended CO_2 working fluids as key to making CSP more competitive against other forms of electrical power generation. The overarching goal of the SCARABEUS project is to lower the LCoE of CSP plants to below 96 euro/MWh (30% lower than currently possible). Within the SCARABEUS project it is necessary to identify optimal cycles and to design the main system components, including the turbomachinery and heat exchangers.

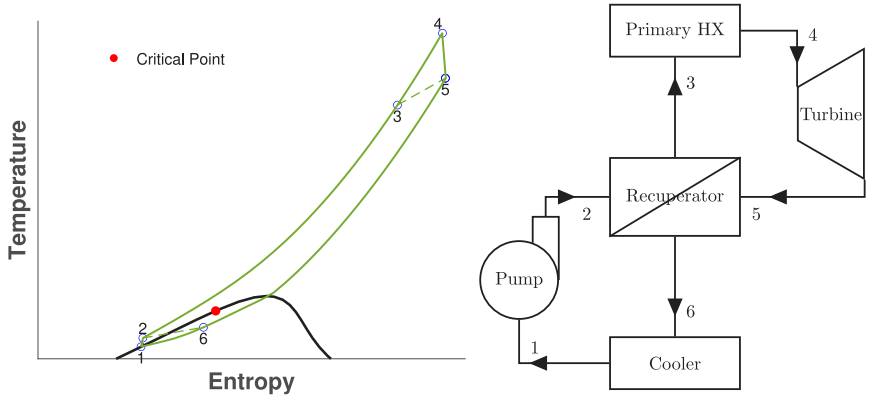

Fig. 1. *T-s* diagram and schematic of a simple recuperated tCO_2 cycle.

The path to commercial realisation of CO_2 power cycles requires the development of key components such as the turbomachinery and heat exchangers. Previous research has determined that turbine performance has a significant influence on the overall cycle efficiency [18–20]. In the case of Novales et al. [19] it was found that sCO_2 Brayton cycles can only compete with state-of-the-art steam cycles at elevated turbine efficiencies above 92%. They also estimated that a 1% efficiency change in the turbine leads to 0.31 – 0.38% change in cycle efficiency depending on cycle type and conditions. While Allison et al. [20] put the figure at around 0.5% cycle efficiency for every 1% turbine efficiency.

The aim of the current work is to investigate the sensitivity of key cycle and turbine design parameters to dopant type and amount within a simple recuperated cycle layout. The chosen dopants are $TiCl_4$, C_6F_6, and an unnamed Non-Organic Dopant (henceforth referred to as NOD). These are among the dopants selected as preliminary candidates by the SCARABEUS project. The chemical formula of NOD will not revealed in this work because it remains confidential within the project consortium. To the authors' knowledge, there has not been any prior investigations of the turbine design sensitivity to dopant fraction. Consequently, this paper aims to provide a description of the dopant effects, and most importantly, to determine if turbine design is insensitive enough to allow the use of pure CO_2 fluid properties during the design process instead of the blends.

The cost and challenges of incorporating CO_2-based mixtures as working fluids in power cycles as a whole are not addressed in this work. This aspect was the focus of other works [14]. Moreover, the thermal stability of these dopants under high temperature (700 °C) and pressure (25 MPa) conditions requires investigation, but will not be dealt with here.

2. Methodology

2.1. Cycle model

In-line with the previous study by Manzolini et al. [14], a simple recuperated tCO_2 cycle was chosen for the purpose of this study. Cycle thermodynamic analysis assumes the following:

- The changes in kinetic and potential energy are negligible.
- Components operate under steady conditions.
- The pump and turbine have fixed isentropic efficiencies.
- The pressure drop in both sides of a heat exchanger is divided proportionally to the heat duty.
- Heat loss to the surroundings is negligible.

A schematic of the tCO_2 cycle and its Temperature–Entropy (*T-s*) diagram are shown in Fig. 1. The cycle is modelled by applying the first law of thermodynamics to all equipment. Compression and expansion work are expressed by Eqs. (1) and (2):

$$w_p = h_2 - h_1 \tag{1}$$

$$w_t = h_4 - h_5 \tag{2}$$

where w_p and w_t are the specific compression and expansion work, respectively, and h_i is the enthalpy at point 'i' in the cycle. The difference between the expansion and compression work is defined as the net specific work output, and is expressed by Eq. (3):

$$w_n = w_t - w_p \tag{3}$$

Once the cycle output work capacity $\dot{W}_n$ is set, the net specific work is used to find the mass flow rate of the working fluid using Eq. (4):

$$\dot{m} = \dot{W}_n / w_n \tag{4}$$

Heat loads in the primary heat exchanger, recuperator and cooler are expressed by Eqs. (5) to (7):

$$q_H = h_4 - h_3 \tag{5}$$

$$q_R = h_3 - h_2 = h_5 - h_6 \tag{6}$$

$$q_L = h_6 - h_1 \tag{7}$$

Cycle thermal efficiency is expressed as the ratio of the net work produced to the heat consumed by the cycle in Eq. (8):

$$\eta_o = \frac{w_t - w_p}{q_H} \tag{8}$$

The losses within the pump and turbine are approximated by assuming isentropic efficiencies for each component, as expressed by Eqs. (9) and (10):

$$\eta_p = \frac{h_{2s} - h_1}{h_2 - h_1} \tag{9}$$

$$\eta_t = \frac{h_4 - h_5}{h_4 - h_{5s}} \tag{10}$$

where the subscript 's' denotes the outlet conditions assuming isentropic compression and expansion.

The recuperator effectiveness determines the ratio of the actual heat load to the maximum attainable heat load from the stream with the lowest heat-capacity rate, as expressed in Eq. (11):

$$\epsilon = \frac{q_R}{q_{R,max}} = \frac{h_5 - h_6}{\min\left[\left(h_{@T5,P2} - h_{@T2,P2}\right), \left(h_{@T5,P5} - h_{@T2,P5}\right)\right]} \tag{11}$$

An internal pinch point is expected in the recuperator, which must be determined to avoid physically impossible (overlapping) temperature profiles. In order to do so, the recuperator is discretised into cells,

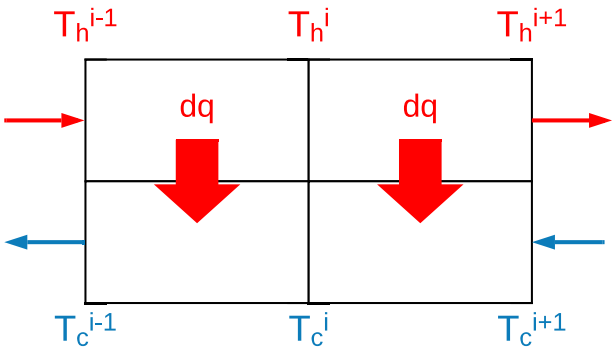

Fig. 2. Illustrative example of recuperator discretisation.

as shown in Fig. 2, each with an equal heat load. The pressure drop is also assumed to be equally divided along all nodes, although this is not entirely representative since the transport properties of the fluids and the length of each segment differ. However, because of its trivial effect on the isobaric heat capacity, the variation in pressure drop is not expected to notably change the value of the minimum internal temperature approach (MITA). The first law is then applied between the nodes to calculate the change in enthalpy based on the exchanged heat. Finally, the enthalpy and pressure are fed into the Equation of State (EoS) to calculate the temperature at each node.

The recuperator is sized based on its overall conductance. The overall conductance is defined for each node as:

$$UA = Q/LMTD \tag{12}$$

where UA is the overall conductance, Q is the heat load for each cell, and $LMTD$ is the log mean temperature difference between its terminals, which is expressed as:

$$LMTD = \frac{(T_h^i - T_c^i) - (T_h^{i+1} - T_c^{i+1})}{\ln((T_h^i - T_c^i)/(T_h^{i+1} - T_c^{i+1}))} \tag{13}$$

The error in the calculated MITA is dependent on the chosen number of cells. It was found that dividing the recuperator into 50 cells results in $< 2\%$ error for all mixtures at all blend fractions.

The pressure ratio across the turbine is defined as:

$$r = P_4/P_5 \tag{14}$$

where and P_4 and P_5 are the inlet and outlet total pressures, respectively.

The cycle state points are determined by setting the pump inlet temperature (T_1), the turbine inlet temperature (T_4), pressure ratio, component efficiencies, and pressure drops. Within this study, T_1 and T_4 will be set according to the values expected in state-of-the-art dry-cooled CSP plants. Whilst the recuperator effectiveness and the turbine pressure ratio are the two variables that will be tuned to optimise the cycle thermal efficiency, as will be explained in Section 2.3.

2.2. Turbine model

To model the turbine, a preliminary mean line turbine design approach was adopted. The target net power for the SCARABEUS plant is 100 MW turbine, for which a multi-stage axial architecture is recommended [21]. For such a compressible flow axial turbine, the optimal specific speed range is from 0.4 to 1.0 (rad/s) [22]. The specific speed is defined as:

$$\omega_s = \frac{\omega \dot{V}_5^{\frac{1}{2}}}{\Delta h_{ss}^{\frac{3}{4}}} \tag{15}$$

where ω_s and ω are the specific speed and nominal speed (rpm), respectively. The turbine exhaust volume flow rate is represented by $\dot{V}_5$ (in m^3/s) and the isotropic enthalpy drop by Δh_{ss} (in J/kg).

The blade-loading coefficient, turbine flow coefficient, and degree of reaction given by Eqs. (16) to (18) are non-dimensional turbomachinery design parameters that indicate the required blade speed, fluid axial velocity, and proportion of expansion that occurs within the rotor. These parameters are widely used to predict and optimise the axial turbine's performance. Optimal values for these parameters are readily reported within the literature for large-scale turbines operating with steam or air [23]. These values can be readily used to provide a preliminary assessment of turbine design. The design parameters are defined as follows:

$$\psi = \Delta h_{oi}/U_i^2 \tag{16}$$

$$\phi = C_{ai}/U_i \tag{17}$$

$$\Lambda = \Delta h_{ri}/\Delta h_{0i} \tag{18}$$

where Δh_{oi} is the total enthalpy drop across i^{th} stage of the turbine, U_i is the blade speed of the rotor of the i^{th} stage at the design radius (mean radius is used in this study), C_{ai} is the axial flow velocity at the rotor outlet of the stage and Δh_r is the enthalpy drop across the rotor of the i^{th} stage. Further details on the design methodology and a previous validation study that has been conducted are reported in Salah et al. [24].

The number of turbine stages is determined by mechanical considerations, namely the maximum allowable stresses on the rotor blades. Mechanical stresses are approximated by assuming Inconel 740H blade material. Based on manufacturer's data, the ultimate tensile strength of Inconel 740H is 912 MPa at 700 °C [25]. Moreover, an allowable stress limit to endurance strength ratio of ($S_a/S_e = 73/240$) is approximated based on 0.2% creep strain and a 10 000 h fatigue life for an uncooled turbine. To construct the modified Goodman-line, a safety factor of ($n = 1.5$) is assumed. These assumptions are used in Section 3.5 to determine the number of stages in a turbine design case study.

2.3. Optimisation model

A *MATLAB* program was developed to study the sensitivity of the optimal cycle and turbine design to the selected blend. The sensitivity analysis flowchart in Fig. 3 shows two layers of optimisation corresponding to the dopant molar fraction and the two design variables; pressure ratio and recuperator effectiveness. The layers are embedded within each other, meaning that an increment in the dopant molar fraction restarts the optimisation of the design variables. Once optimum cycle conditions for a given mixture composition were found, the program then produces a turbine geometry using the turbine boundary conditions resulting from the optimal cycle. To calculate the thermodynamic and transport properties of the working fluids, *Simulis Thermodynamics* – a commercial software – was used [26].

Within *Simulis Thermodynamics*, the Peng–Robinson (PR) EoS was selected because it is considered to be a reliable yet simple model that is fit for purpose [27]. Representation of the mixtures can be achieved by coupling PR EoS with a mixing model; the Van der Waals model in this case. To account for non-ideal behaviour, the Binary Interaction Parameter (k_{ij}) was derived from empirical data and used to tune the mixing model.

Simulis Thermodynamics was validated through a simple recuperated cycle model for pure compounds and mixtures, respectively. A pure CO_2 cycle was simulated via a REFPROP-based code developed in-house, while data obtained using Aspen Plus for modelling of CO_2-$TiCl_4$ mixture was obtained from Manzolini et al. [14]. The present model showed results consistent with those from REFPROP and Aspen with percentage variation of 0.5% in efficiency (0.2% nominal efficiency variation).

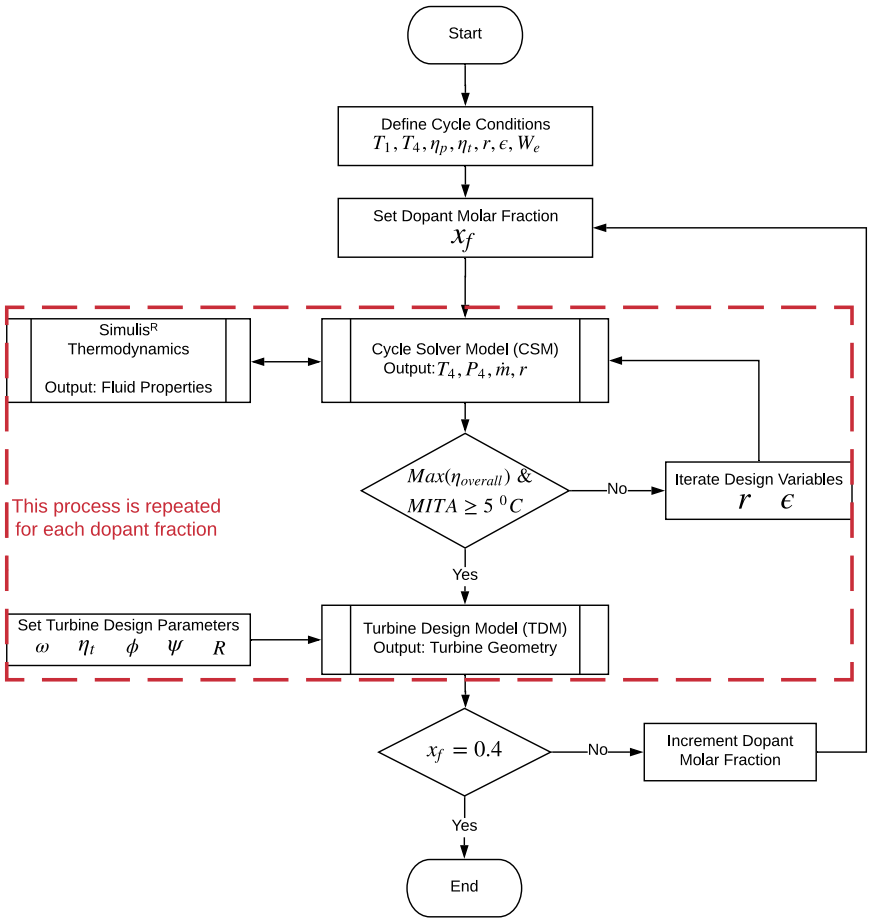

Fig. 3. Flowchart of optimisation model.

Table 1
Physical and thermodynamic properties of pure compounds (calculated using Simulis Thermodynamics).

Compound	Molecular weight (g/mol)	Acentric factor	Critical temperature (K)	Critical pressure (MPa)	Ideal specific heat at $T_r = 2$ (J K^{-1} mol^{-1})
CO_2	44.01	0.2236	304.2	7.382	47.34
$TiCl_4$	189.7	0.2837	639.1	4.661	107.2
NOD	60>	0.23>	400>	7.5>	50>
C_6F_6	186.1	0.3953	516.7	3.273	272.1

2.4. Choice of dopants

The mixtures studied in this paper are among the candidates that have been identified by the SCARABEUS project as potential dopants for CO_2 based power cycles operating within CSP. The main dopant thermophysical parameters of interest are shown in Table 1.

In this study, k_{ij} was calculated against regressed Vapour–Liquid Equilibrium (VLE) empirical data and used to tune the mixing models of CO_2/NOD and CO_2/C_6F_6. Unlike the other two mixtures, the k_{ij} value for CO_2/$TiCl_4$ was taken directly from literature. This is because the lack of experimental data means any recalibration of k_{ij} for CO_2/$TiCl_4$ will retain a high uncertainty margin. In such a case, sensible comparison between the original and the new k_{ij} values will not be possible.

Determining the value of k_{ij} required an optimisation problem. By tuning k_{ij}, the calculated VLE lines were manipulated and compared with experimental data to find the best-fit k_{ij} value. An unconstrained gradient-based optimisation approach was used. The weighted least mean square method was used as the objective function. Like the simple least square method, it minimises the residuals between experimental and calculated data, but it also weighs each residual with the experimental uncertainty of the experimental data. The objective function is reduced or expanded depending on the availability of experimental data. The objective function for the optimisation is defined as:

$$f(k_{ij}) = \frac{1}{n_e}\sum_{i=1}^{n_e}\left(\frac{\hat{x}_{1,i} - \tilde{x}_{1,i}}{u^e_{x_{1,i}}}\right) + \left(\frac{\hat{y}_{1,i} - \tilde{y}_{1,i}}{u^e_{\hat{y}_{1,i}}}\right) + \left(\frac{\hat{T}_i - \tilde{T}_i}{u^e_{\hat{T}_i}}\right) + \left(\frac{\hat{P}_i - \tilde{P}_i}{u^e_{\hat{P}_i}}\right) \quad (19)$$

where x_1 and y_1 are the liquid and vapour molar fractions of CO_2, respectively. The accents ($\wedge$) and ($\sim$) indicate the measured and calculated values, respectively. Experimental uncertainty is represented by the term u^e. The number of experiments is denoted by n_e.

A Monte Carlo technique similar to that used by Hajipour et al. [28] was employed to estimate the uncertainties of the binary interaction parameters. The four main steps in applying this technique are: (1) specification of probability density functions for the uncertain input variables involved in the study based on the knowledge of their uncertainty; (2) probabilistic sampling of the uncertainty space; (3) simulation and calculation of output parameters by passing each sample set through the model; and (4) statistical analysis of the results to evaluate the uncertainty of the model outputs.

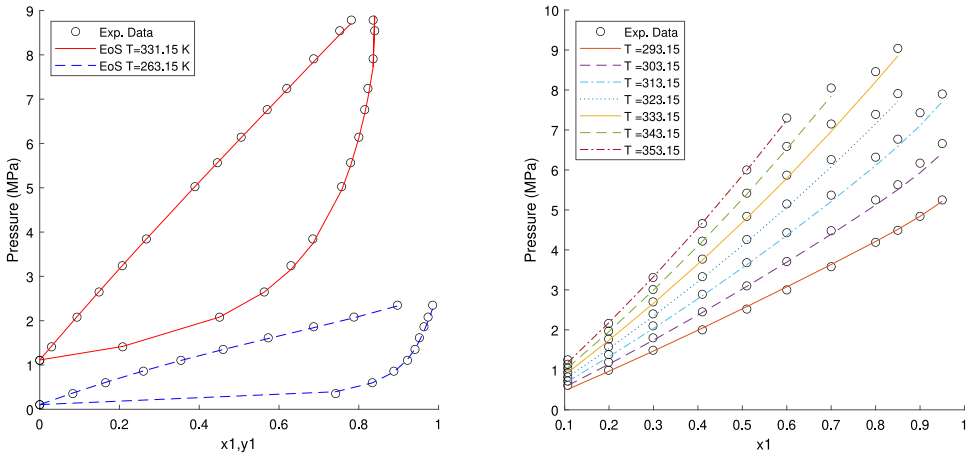

Fig. 4. Phase diagrams for the mixture CO_2/NOD (left) and CO_2/C_6F_6 (right). Lines represent the results of PR EoS with (k_{ij} = 0.0243) and (k_{ij} = 0.0312) for CO_2/NOD and CO_2/C_6F_6, respectively. Whilst the circles are the experimental data points taken from their respective sources.

Table 2
Optimised BIP with uncertainty intervals.

Mixture	k_{ij}	Uncertainty	Source of data
$CO_2/TiCl_4$	0.0745	± 0.0456 (57.6%)	Taken from Bonalumi et al. [27]
CO_2/NOD	0.0243	± 0.0031 (12.8%)	Reference not provided
CO_2/C_6F_6	0.0312	± 0.0104 (33.3%)	Calculated from Dias et al. [29]

In this study, the experimental data were assumed to be normally distributed in accordance with the declared uncertainty (Step 1). Random sampling with replacement was repeatedly conducted for a total of 1000 trials (Steps 2 & 3). Finally, the mode value is taken as k_{ij}, while its uncertainty is based on the 95% confidence interval from the mean (Step 4). The regressed VLE lines of CO_2/NOD and CO_2/C_6F_6 are shown in Fig. 4. The values of k_{ij} adopted in this study are shown in Table 2.

2.5. Optimisation conditions

The pump inlet temperature (T_1) was set to 50 °C. This was chosen to be compatible with dry cooling temperatures in hot arid regions, assuming an ambient dry-bulb temperature of 40 °C. The cooling air is assumed to warm up by 5 °C as it passes through the condenser whilst maintaining a minimum temperature difference of 5 °C [30–33]. The pump inlet was assumed to be subcooled by 2 °C below the saturation pressure. Consequently, the pump inlet pressure (P_1) is defined by the saturation pressure of the fluid at 52 °C. The turbine inlet temperature (T_4) was set to 700 °C, which is targeted by an advanced CSP receiver employing sodium salt as its Heat Transfer Medium (HTM). Additionally, the turbine inlet pressure (P_4) was restricted to 25 MPa as recommended by Dostal et al. [18].

To prevent the dopant from becoming the dominant compound in the mixture, the maximum molar fraction of the dopant was set to 0.40. The minimum dopant molar fraction was assumed to be the value at which the critical temperature of the mixture is equal to, or slightly exceeds 57 °C (40 °C heat sink temperature + 10 °C cooler temperature difference + 2 °C sub-cooling + 5 °C margin from the critical temperature). A summary of the assumptions is provided in Table 3.

Table 3
Inputs required for cycle solution.

Controlled parameters			
Parameter		Range	Unit
Dopant molar fraction	X_f	Max(0.4)	%
Turbine inlet temperature	(T_4)	700	°C
Pump inlet temperature	(T_1)	50	°C
Pump isentropic efficiency	(η_p)	85	%
Turbine isentropic efficiency	(η_t)	90	%
Generator efficiency	(η_g)	99	%
Minimum internal temperature approach	(MITA)	5	°C
Net electrical power	(W_e)	100	MW
Pressure drop in primary heat exchanger	$\Delta p/p$	0.015	–
Pressure drop in recuperator High- and Low-pressure sides	$\Delta p/p$	0.01 and 0.015	–
Pressure drop in condenser	$\Delta p/p$	0.02	–
Dependent parameters			
Pump inlet pressure	(P_1)	$P_{sat@(T_1+2)}$	MPa
Turbine inlet pressure	(P_4)	Max (25)	MPa
Optimised parameters			
Pressure ratio	(r)	2 to Max (P_4)/P_1	–
Recuperator effectiveness	(ϵ)	80 to 98	%

3. Results and discussion

In order to fully capture the effect of mixture composition on the turbine design, it is helpful to first examine its effect on the cycle parameters as a whole. Analysis of the results will first investigate cycle behaviour, with emphasis on turbine boundary conditions and the expansion process. Then, the change in working fluid characteristics and their expected effect on the cycle and turbine design is considered. After which, turbine geometries for the SCARABEUS project case study will be discussed in more detail. Henceforth, any observations on parameter trends will be in reference to the increase in molar fraction of the dopant, unless stated otherwise. Moreover, a uniform graphical representation of the three mixtures is adopted throughout the proceeding sections as introduced in Fig. 5.

The critical loci of the binary mixtures are illustrated in Fig. 5. There is a notable difference in the shape of the critical locus of each mixture. The shape indicates the evolution of the Liquid–Vapour coexistence lines with changing composition. Since the minimum cycle pressure in a transcritical cycle is determined by the condensation pressure at the prescribed minimum temperature, the shift in the coexistence line defines a new equilibrium condensation pressure, which ultimately influences the cycle's pressure ratio. In general, as the critical pressure increases, the vapour pressure of the fluid increases, thus decreasing the cycle pressure ratio for a fixed maximum turbine inlet pressure. Whereas an increase in the critical temperature decreases the vapour pressure of the fluid and increases the cycle's pressure ratio. The change in vapour pressure is also proportional to its position relative to the critical point, and is greatest near the critical point. It is the interplay between these factors that eventually determines the aggregate change in vapour pressure, namely the pump inlet pressure.

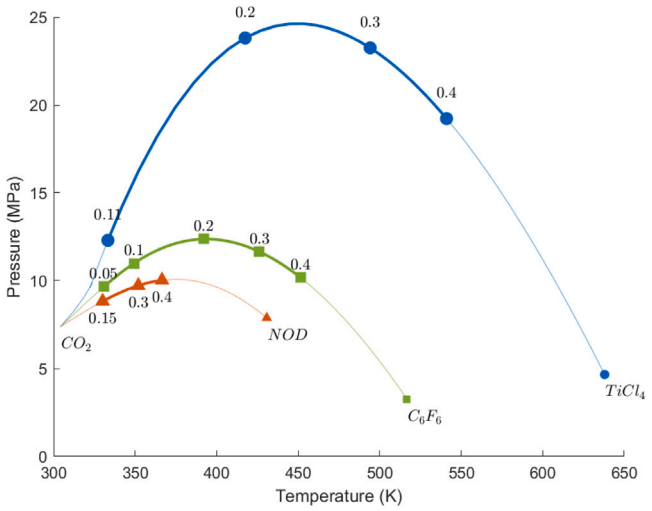

Fig. 5. The highlighted segments represent the critical loci corresponding to the blend fractions studied for each mixture. The point labels indicate the dopant molar fraction at that point. The same styling convention is used to differentiate the three mixtures in all subsequent figures.

3.1. Cycle analysis

The pump inlet pressures decrease as the dopant fractions increase as seen in Fig. 6. Consequently, the decrease in condensation pressure induces an increase in the cycle pressure ratio in order to achieve higher levels of cycle thermal efficiency. The fall in condensation pressure is directly proportional to the increase in pressure ratio; which is greatest in CO_2/C_6F_6.

The trend in efficiency exhibits an optimal point for each mixture, as seen in Fig. 7. The dopant molar fractions corresponding to the points of maximum efficiency are 0.174, 0.264, and 0.167 for mixtures of $CO_2/TiCl_4$, CO_2/NOD, and CO_2/C_6F_6, respectively. Among the three blends, $CO_2/TiCl_4$ achieves the highest thermal efficiency of 49.5%, followed by CO_2/C_6F_6 with an optimal thermal efficiency of 46.5%, while CO_2/NOD achieves the lowest efficiency of 42.3%. Although not shown in the figure, simulation of an equivelant pure CO_2 cycle achieves thermal efficiency of 44.0%. The 7.2% difference in efficiency between $CO_2/TiCl_4$ and CO_2/NOD cycles highlights the significant influence the choice of dopant has on cycle performance. These dopant molar fractions will later be used to compare the turbine geometries of the three mixtures.

The trend in efficiency is a consequence of the change in the net shaft work ($w_t - w_p$) and the primary heat exchanger heat load, which in turn is affected by the change in recuperated heat. By inspection of the rate of change of the two parameters (net specific work and PHE heat load) with the dopant fraction, the change in efficiency becomes clearer. For CO_2/NOD, both parameters increase at roughly the same rate, thus maintaining a fairly constant efficiency with dopant fraction. For CO_2/C_6F_6 the PHE heat load decreases at a decreasing rate while the net specific work decreases at an almost constant rate. Therefore, the cycle efficiency exhibits an inversion point of maximum efficiency after which the PHE heat lead decreases at a rate lower than that of the net specific work, which causes efficiency to drop. The same applies to $CO_2/TiCl_4$, but the drop in efficiency is more dramatic because the net specific work decreases at an increasing rate.

On the other hand, the trend in the net work is mainly driven by the change in the specific work, as seen in Fig. 11. Similar to a pure sCO_2 cycle, cycles operating with CO_2 based mixtures are highly recuperative. As shown in Fig. 7, the recuperated heat is much greater than the primary heat exchanger load for all mixture compositions. This is because of the relatively low pressure ratios and specific work across the turbine, which accompany higher turbine outlet temperatures. Recuperated heat is 3.2 to 3.5 times greater than the primary heat exchanger load for $CO_2/TiCl_4$, 2.3 to 4.0 times greater for CO_2/C_6F_6, and 1.6 to 1.8 times greater for CO_2/NOD.

As the recuperator effectiveness increases, the MITA in the recuperator decreases. Therefore, the recuperator effectiveness is reduced to maintain a MITA of around 5 °C, whilst achieving optimal cycle thermal efficiency. Fig. 8 shows the reduction in effectiveness with increasing dopant fractions. It was found that CO_2/NOD exhibits an abrupt fall in recuperator effectiveness for dopant molar fractions above 0.26, which corresponds to the NOD molar fraction above which condensation occurs in the recuperator. The same effect is illustrated in Fig. 7 where the recuperated heat rises abruptly at the same NOD molar fraction.

The well-matched temperature profiles and higher effectiveness comes at the cost of larger recuperators. The overall conductance values of the entire recuperator are indicative of its size and were obtained by adding the overall conductance of each of its discrete cells (see Fig. 2). As seen in Fig. 8, the overall conductance of the two heavy mixtures – $CO_2/TiCl_4$ and CO_2/C_6F_6 – are much higher than CO_2/NOD. The trend in overall conductance with dopant molar fraction is mainly attributed to the change in the temperature profiles of the two streams, indicated by the average LMTD, also shown in Fig. 8. The greater the LMTD the smaller is the recuperator.

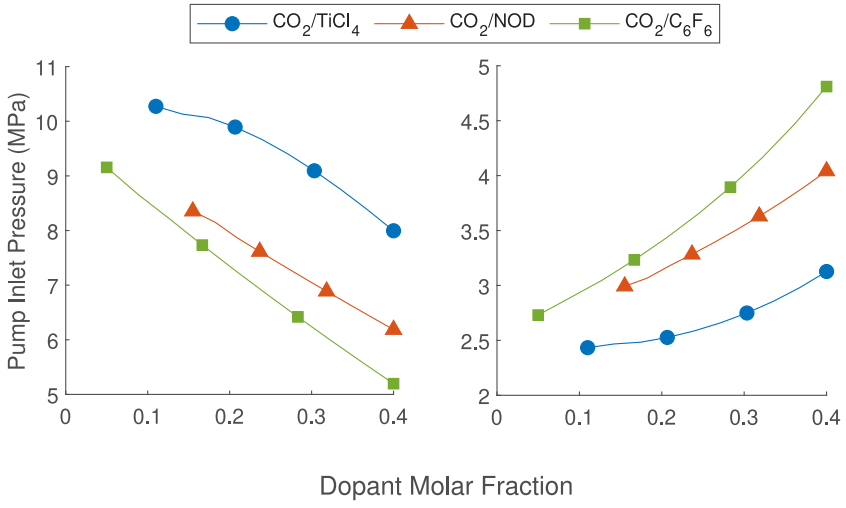

Fig. 6. Variation of pump inlet pressure and pressure ratio with dopant molar fraction.

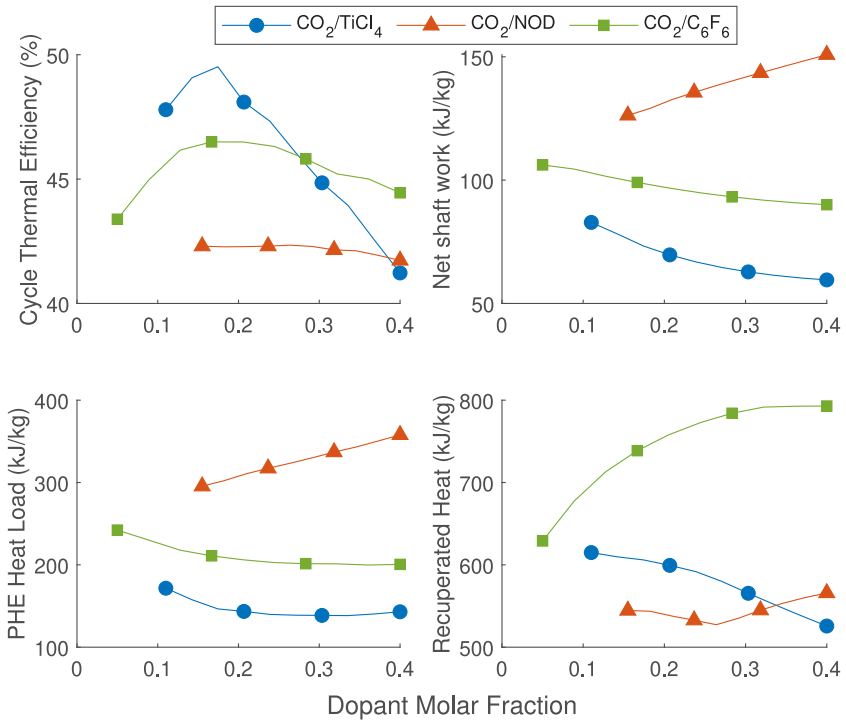

Fig. 7. Variation of cycle thermal efficiency, net shaft work, primary heat exchanger load, and the specific recuperated heat with dopant molar fraction.

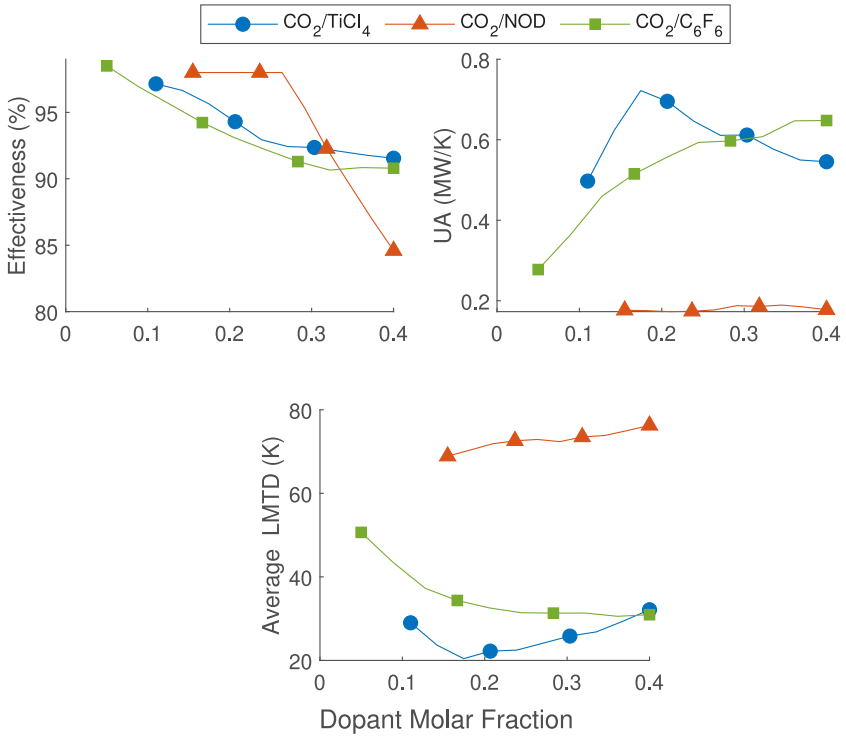

Fig. 8. Variation of recuperator effectiveness and overall conductance with dopant molar fraction.

A survey of the recuperator *T-Q* diagram for the optimal blend of each dopant is shown in Fig. 9. It reveals the difference between the temperature profiles of each blend and the exergy loss (irreversibility) in the recuperator. CO_2/NOD exhibits the greatest irreversibility and poorest match of the two streams; similar to pure CO_2. A proven solution to this issue is the adoption of more complex cycle architectures such as the recompression or partial cooling cycles [16]. The temperature profiles for CO_2/C_6F_6 and $CO_2/TiCl_4$, on the other hand, are well matched. Therefore, these mixtures work well in a simple recuperative cycle, and may not require elaborate cycle configurations, as previously noted by Manzolini et al. [14].

Because their profiles are almost parallel, higher effectiveness in CO_2/C_6F_6 and $CO_2/TiCl_4$ cycles will reduce the exergy loss along the recuperator length, not just at the pinch point. However, using the

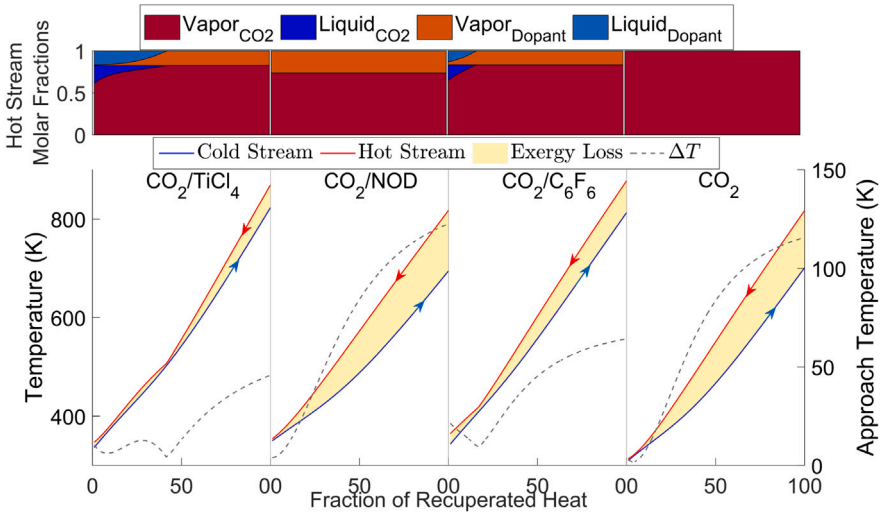

Fig. 9. Temperature versus heat load profile of the recuperator for each working fluid at optimal dopant fraction. The plots at the top indicate the change in the liquid and vapour molar fractions of the hot stream along the recuperator.

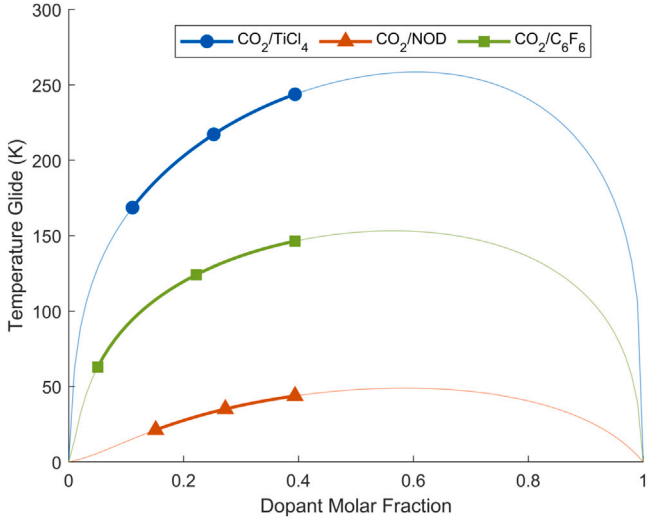

Fig. 10. Difference between bubble and dew temperatures (temperature glide) for all compositions of the three mixtures. the highlighted segments represent the range of molar fractions studied here.

same argument, a CO_2/NOD working fluid would not benefit much from higher effectiveness since it will reduce exergy loss at the pinch point without affecting the majority of the exergy loss elsewhere in the recuperator. Therefore, using a high recuperator effectiveness for all working fluids while discounting the pinch point approach temperature from the analysis gives CO_2/NOD a false advantage. It may also lead to unobserved temperature profile overlaps and the consequent misidentification of the optimal dopant fraction and turbine design point.

Fig. 9 also shows the vapour and liquid compositions of the hot stream within the recuperator. Condensation does not occur in CO_2/NOD mixture at this composition, and is also trivial for all considered fractions of NOD below (0.4). Considerable condensation occurs in both $CO_2/TiCl_4$ and CO_2/C_6F_6 recuperators, where almost 33% and 23% of the heat is exchanged during two-phase flow, respectively. This phenomenon is directly caused by the mixture's temperature glide. As the dew temperature becomes greater than the bubble temperature, the portion of the recuperation process that occurs in the two-phase region increases. Fig. 10, shows the temperature glide during heat rejection for the three working fluids. $CO_2/TiCl_4$ exhibits the greatest temperature glide, followed by CO_2/C_6F_6 and CO_2/NOD. The high degree of glide in the two heavy mixtures suggests that appreciable fractionation (where one component is largely in the vapour state, while the other is still mostly liquid) occurs during cooling, which might require additional equipment such as vapour–liquid separators and separate heat exchangers for each component.

As seen in Fig. 11, the turbine specific work decreases for both $CO_2/TiCl_4$ and CO_2/C_6F_6, but increases for CO_2/NOD; the cause of which will be explained later. For a fixed electrical power output, the change in specific work causes an opposite trend in the mass flow rate. Not only does the turbine exhaust volumetric flow rate depend on the mass flow rate, but it also depends on its density. For all working fluids, the volume flow rate decreases with dopant fraction because of the increase in the fluids' density.

A zero-dimensional study of the specific speed for the whole turbine gives an indication of its shape and size. With a fixed rotational speed, any change in the specific speed will be a result of the change in the volumetric flow rate or specific enthalpy drop across the turbine. As seen in Fig. 11 the specific speed of $CO_2/TiCl_4$ and CO_2/C_6F_6 increases with blend fraction, indicating a reduction in the turbine's diameter, accompanied by an increase in the annulus area. The opposite is true for the CO_2/NOD mixture, where wider turbines with smaller annulus areas are expected at higher dopant fractions.

3.2. Incorporation into solar power tower

To compare the adaptability of the optimal working fluids to Solar Power Tower (SPT) applications, the cycles were tested for how well they incorporate a thermal energy storage (TES) system and for their compatibility with dry cooling. Although SPT plants can directly heat the working fluid in the receiver, the use of a TES system presents operational and economic advantages. Therefore, it should be considered when comparing between cycles.

An indicative TES size comparison was obtained by assuming a constant temperature difference between the heat transfer medium (HTM) and the working fluid at both terminals of the primary heat exchanger (PHE). Consequently, the change in the working fluid and HTM temperatures across the PHE are equal. Moreover, with a constant HTM specific heat capacity, Eq. (20) describes the relation between the HTM mass (m_{HTM}), the cycle heat input (Q_H), and the rise in the working fluid's temperature across the PHE (ΔT_{PHE}).

$$m_{HTM} = Q_H/(C_p \Delta T_{PHE}) \quad (20)$$

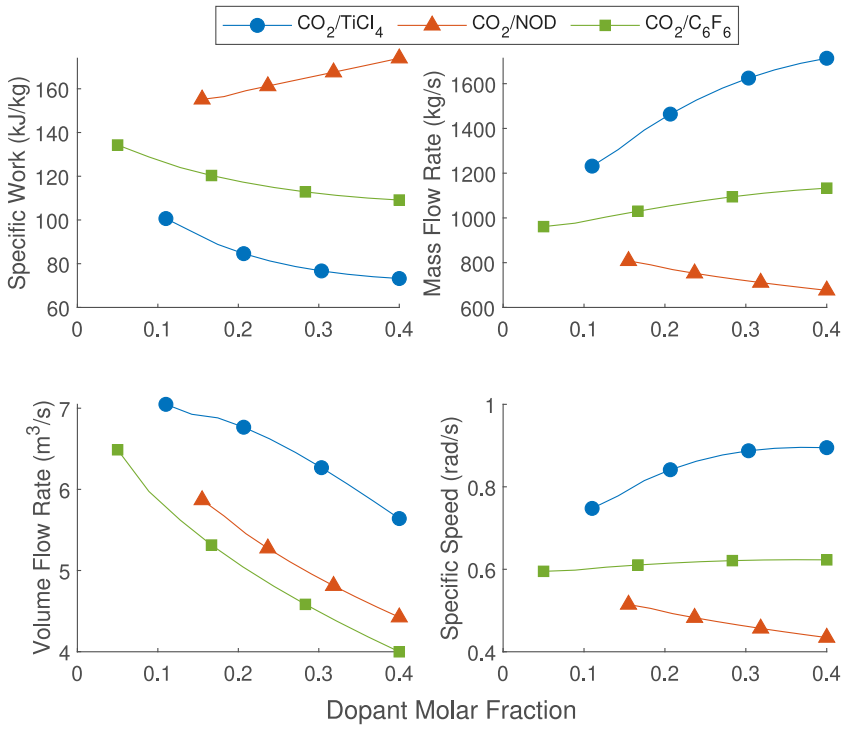

Fig. 11. Variation of turbine specific work, mass flow rate, volume flow rate at turbine outlet, and specific speed with dopant molar fraction.

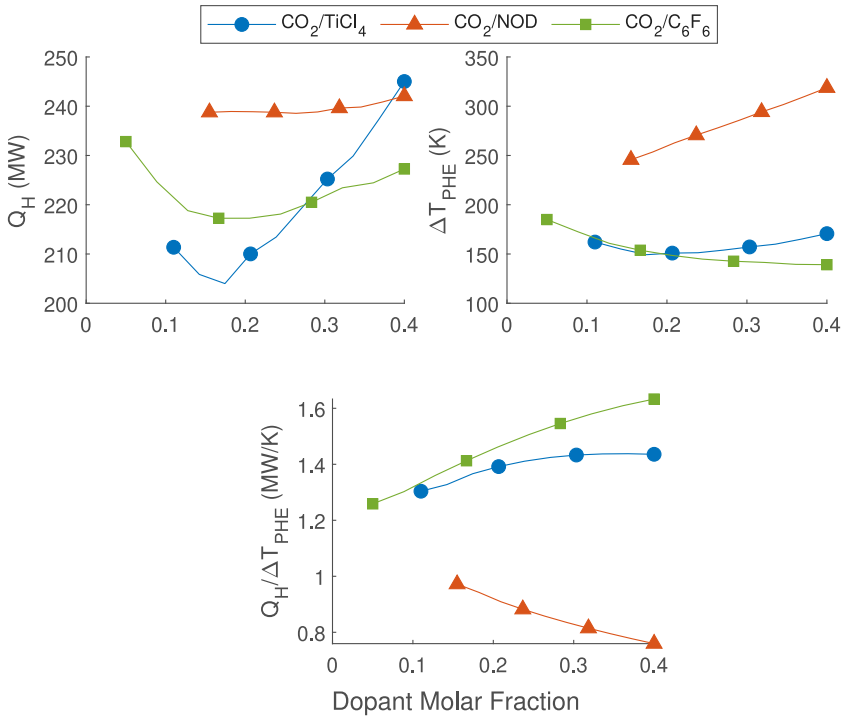

Fig. 12. Thermal energy storage size indication.

As previously established, CO_2/NOD is the least recuperative of the three mixtures because it requires the highest heat input, as seen in Fig. 12. However, for the same reason, it exhibits the highest temperature difference across the PHE. Therefore, greater sensible heat is extracted from the HTM with CO_2/NOD. This manifests in the overall effect on TES size, which is indicated by the ratio $Q_H/\Delta T_{PHE}$, and is the lowest for CO_2/NOD. Between the remaining two mixtures, the ratio is around 1.4 MW/K for the optimal blend fractions of 0.174 and 0.167 for $CO_2/TiCl_4$ and CO_2/C_6F_6, respectively. Nevertheless, CO_2/C_6F_6 will require larger TES at higher dopant fractions.

Variations in ambient temperature affect the condenser's ability to remove heat from the cycle, which will change the temperature of the working fluid at pump inlet. The more susceptible the performance of the cycle is to variations in the pump inlet temperature, the less compatible it is with dry cooling.

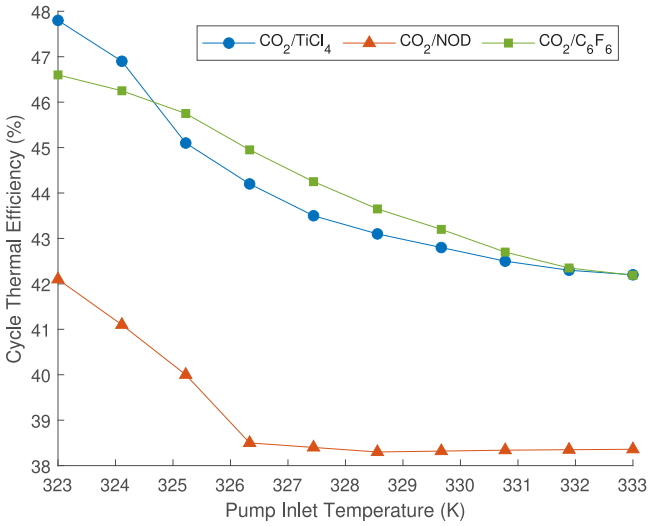

Fig. 13. Change in thermal efficiency with pump inlet temperature variations.

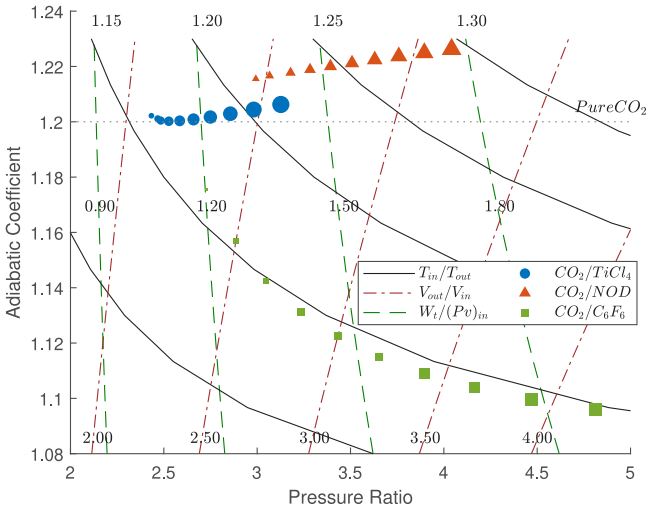

Fig. 14. Maps the effect of dopant fraction on the turbine isentropic volume, temperature, and pressure ratios. The size of the point is proportional to the dopant fraction.

Logically, the rise of ambient temperatures above the 40 °C design point is the main concern, since a drop in ambient temperatures is likely to improve the cycle's performance, and can even be mitigated by controlled cooling, if need be. However, an elevation in the cooling air temperature cannot be easily mitigated, thus it will affect the condenser's performance. Fig. 13 reveals the loss in efficiency as the pump inlet temperature is increased by up to 10 K. The efficiency for each temperature increment is obtained by rerunning the optimisation at the elevated turbine inlet temperatures. Although, all three mixtures exhibit about 4% loss in efficiency, the effect is less pronounced in $CO_2/TiCl_4$ and CO_2/C_6F_6 because it occurs gradually over the 10 K range. Conversely, the 4% loss occurs within an increment of only 3 K for CO_2/NOD. This is a consequence of the pump inlet conditions growing closer to the critical point where the fluid becomes more compressible, thus requires greater compression work.

3.3. Expansion process

To characterise the expansion process, Figs. 14 and 15 have been derived by assuming ideal gas behaviour throughout the expansion process and using the isentropic relations shown in Eqs. (21) and (22):

$$r = \frac{P_{in}}{P_{out}} = \left(\frac{T_{in}}{T_{out}}\right)^{\frac{\gamma}{\gamma-1}} = \left(\frac{v_{out}}{v_{in}}\right)^{\gamma} \tag{21}$$

$$w_t = \eta_t \left(\frac{\gamma}{\gamma-1}\right) \frac{P_{in}}{\rho_{in}} \left(1 - r^{\frac{1-\gamma}{\gamma}}\right) \tag{22}$$

where γ is the adiabatic coefficient ($\gamma = C_p/C_v$). The assumption of ideal gas behaviour easily permits an investigation of certain flow features without the aid of a more sophisticated EoS. This assumption is justified by the near unity (0.95 to 1.1) compressibility factor of all working fluids at both turbine inlet and outlet.

As shown in Fig. 14, the adiabatic coefficients of $CO_2/TiCl_4$ and CO_2/NOD increase modestly, but significantly decrease for CO_2/C_6F_6. The trend in the adiabatic coefficient of CO_2/C_6F_6 is almost coincident with the isoline $T_1/T_2 = 1.15$, indicating that the decrease in the isentropic coefficient negates the effect of the increase in pressure ratio on the temperature drop across the turbine, thus maintaining almost the same temperature drop for all fractions. In contrast, the temperature drop increases for $CO_2/TiCl_4$ and CO_2/NOD, suggesting a reduction in the recuperative capacity of their cycles. This finding agrees with the trends in specific recuperated heat shown in Fig. 7.

The expansion ratio of the CO_2/C_6F_6 increases at a higher rate than the other two mixtures because of the more drastic changes in the pressure ratio and in the adiabatic coefficient. Higher expansion ratios indicate greater compressibility effects, as confirmed by Fig. 17. Therefore, CO_2/C_6F_6 turbines may be more susceptible to supersonic flows than the other two mixtures, and are also likely to exhibit larger blade height variations in multi-stage turbines as the amount of C_6F_6 increases. This is explored in the next section.

By rearranging Eq. (22), the relation between specific work and adiabatic coefficient can be described through the work to pressure–volume ratio, as seen in Eq. (23).

$$\frac{w_t}{(Pv)_{in}} = \eta_t \left(\frac{\gamma}{\gamma-1}\right) \left(1 - r^{\frac{1-\gamma}{\gamma}}\right) \tag{23}$$

The fixed density-specific work isolines in Fig. 14 depict the relative independence of specific work from the adiabatic coefficient. At its greatest, the drop in the adiabatic coefficient of CO_2/C_6F_6 causes a mere 3% drop in specific work, whereas its effect on the specific work for the other two mixtures is less than 1%. Overall, Fig. 14 suggests that the adiabatic coefficient becomes more significant at higher pressure ratios. Therefore, if the maximum allowable cycle pressure is increased, the variances between the expansion processes of the mixtures are expected to become more pronounced.

The effect of the density at turbine inlet is evident in Fig. 15. Whilst ignoring the effect of the change in the adiabatic coefficient on specific work, which has been shown to be trivial, higher densities result in lower specific work for a given pressure ratio. In the present study, both density at turbine inlet and pressure ratio increase with dopant molar fraction, but to varying degrees. For CO_2/NOD the increase in density is small, thus the specific work increases with the increasing pressure ratio. For $CO_2/TiCl_4$ and CO_2/C_6F_6, however, there is a significant increase in density which causes a decrease in the specific work, even though the pressure ratio increases. For comparison, the densities of $CO_2/TiCl_4$, CO_2/NOD, and CO_2/C_6F_6 increase by 74%, 11%, and 91%, whilst the pressure ratios increase by 28%, 35%, and 76%, respectively. The outcome is a 27% and 19% decrease in specific work for $CO_2/TiCl_4$ and CO_2/C_6F_6, and an increase of 12% in specific work for CO_2/NOD. These results demonstrate the dependence of specific work on both density and pressure ratio, which are in turn dependent on the dopant molar fraction.

The same phenomena may also be observed through the slope of the expansion isentrope in a *P-h* diagram and in Eq. (24). In Fig. 16, the slope of the isentrope depends on the fluid density while the horizontal

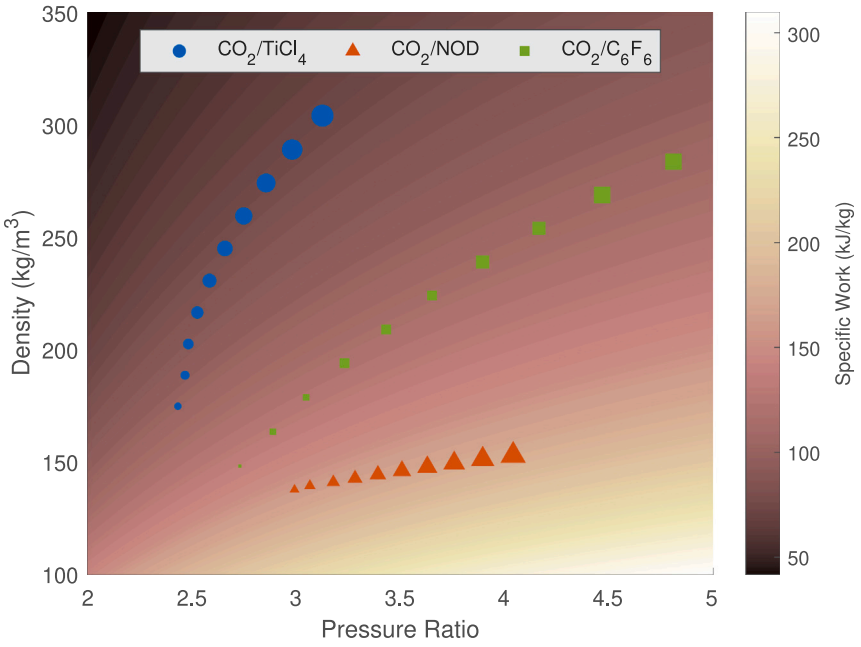

Fig. 15. Maps the effect of dopant fraction on the working fluid's density at turbine inlet, pressure ratio, and turbine specific work. The size of the point is proportional to the dopant fraction.

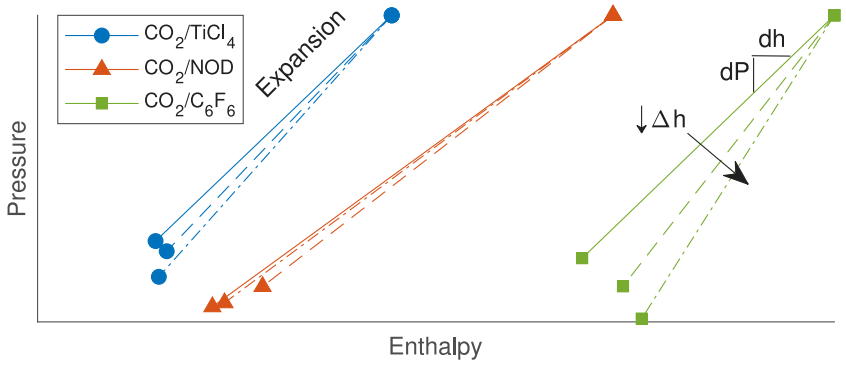

Fig. 16. Compares between the expansion process for three different amounts of dopant fractions. The solid line (-) indicates low dopant fraction, the dashed line (- -) indicates medium dopant fraction, and the dot–dash (-.) line indicates high dopant fraction.

distance between the two ends of the expansion process indicates its specific work.

$$dh = Tds + dP/\rho \xrightarrow{ds=0} dh = dP/\rho \tag{24}$$

As the molar fraction of the dopant increases, the slope and lower end of the expansion process changes according to the turbine inlet density and pressure ratio, respectively. Since the density of all mixtures increases with blend fraction, their expansion follows a steeper isentrope. Simultaneously, the increasing pressure ratio extends the vertical length of the line. The combined movements of the two effects ultimately determines the horizontal distance (enthalpy drop). The same effect may be attained by lowering the turbine inlet temperature and moving closer to the Andrew's curve where densities are higher.

3.4. Molecular characteristics

As shown in Fig. 17, the molecular weight of the working fluid increases significantly with the addition of C_6F_6 or $TiCl_4$, but only slightly with NOD. Higher molecular weights are known to decrease the heat transfer coefficient and increase the size of the heat exchangers [34]. Since the turbine inlet temperature is constant, and the effect of the isentropic coefficient is minor, the increase in molecular weight leads to an increase in density and a decrease in the speed of sound according to Eqs. (25) and (26):

$$a = \sqrt{\gamma RT/M} \tag{25}$$

$$\rho = PM/RT \tag{26}$$

where the fluid is assumed to be an ideal gas, a is the speed of sound (m/s), γ is the adiabatic coefficient, M is the molar weight (kg/mol), and R is the ideal gas constant (8.314 J/mol K).

The decrease in the speed of sound is almost identical for the two heavy mixtures $CO_2/TiCl_4$ and CO_2/C_6F_6, while CO_2/NOD exhibits a less dramatic change in the speed of sound. As a general rule, the reduction in the speed of sound in conjunction with the increase in pressure ratio may lead to an increase in Mach numbers and the creation of supersonic flows.

Counter intuitively, $CO_2/TiCl_4$ is expected to have lower Mach numbers than CO_2/C_6F_6, although it exhibits comparable sound speeds. This contrast is attributed to the particulars of the overall cycle behaviour which limit the pressure drop of $CO_2/TiCl_4$ during expansion. Consequently, for the same number of stages, lower Mach numbers are expected in $CO_2/TiCl_4$ than the other two mixtures. However, as will be seen in the next section, subsonic flow requirements are not the determining factor for the number of turbine stages, rather it

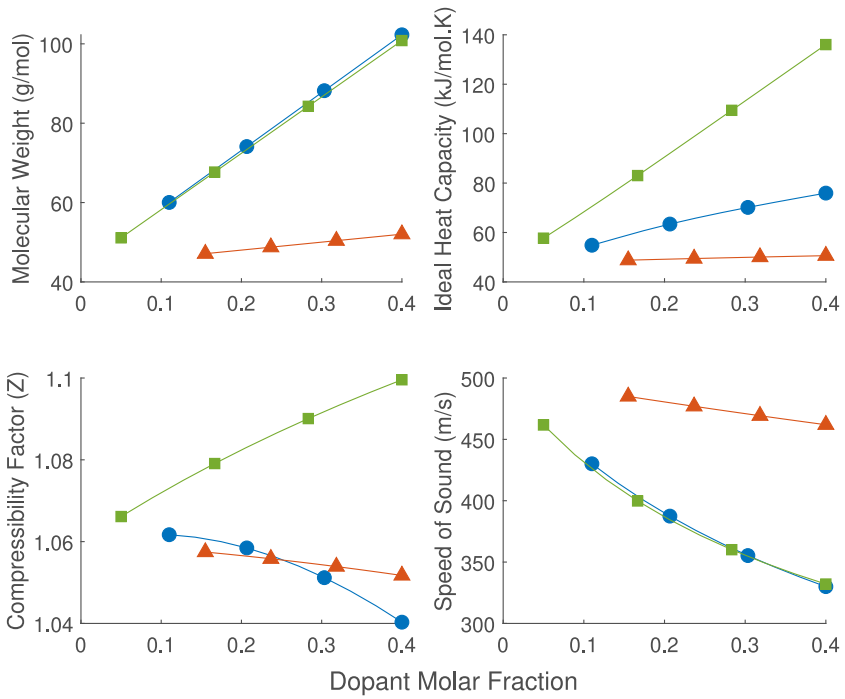

Fig. 17. Variation of molecular weight, ideal specific heat capacity, compressibility factor at turbine inlet, and speed of sound at turbine inlet with dopant molar fraction.

is the maximum allowable blade stress. Therefore, it is unlikely that supersonic flow conditions will present issues for any of the blends.

The ideal heat capacity, also shown in Fig. 17, is also effected by the dopant molar fraction. It increases for mixtures of CO_2/C_6F_6 and $CO_2/TiCl_4$, but remains almost constant for CO_2/NOD. Ideal heat capacity depends on the molecular complexity of the fluid (number of atoms per molecule and their configurations). From a molecular perspective, this trend may be attributed to the increasing complexity of the mixture molecules with the addition of the dopants. Since NOD has a similar complexity to that of CO_2, there is no tangible change in the mixture's ideal heat capacity.

The ideal heat capacity has profound implications on recuperative cycles. Higher values reduce the difference between the heat capacities of the low- and high-pressure streams of the recuperator. The relative difference between the two has a direct effect on the pinch point temperature and the compatibility of the temperature profiles; i.e. the lower the difference the better the recuperation. The trend in ideal specific heat explains the T-Q profiles and irreversibilities observed in Fig. 9 earlier.

3.5. Mean-line turbine design

The results presented in this section are intended to compare the general trends in the turbine design with dopant molar fraction. Moving into the mean-line design of an axial turbine requires the definition of certain parameters, which are summarised in Table 4. The selection of these parameters was based on common design practices that yield high turbine efficiencies [23]. No attempt has been made to modify these parameters to optimise the turbine designs. Rather, the assumptions were made with the intent of providing a common basis for comparing turbine geometries, regardless of the blend. Further turbine optimisation is required before optimal designs for specific blends are compared, which will be considered in future work.

Within the current paper, as noted in Table 4, the turbine mean-line design relies on the assumption of a fixed turbine efficiency. This was selected since, in our opinion, there remain uncertainties in the suitability of existing loss correlations for operating with both CO_2 and blends. This assumption is deemed sufficient for the objectives of the current study, which is focused more on the overall cycle and general effect of the blend the turbine design, rather than identifying optimal turbine geometries.

Table 4
Turbine design parameters.

Parameter	Value	Units
Rotational speed (N)	3000	RPM
Turbine efficiency (η_t)	90	%
Loading coefficient (ψ)	1.65	–
Flow coefficient (ϕ)	0.23	–
Degree of reaction (Λ)	0.5	–
Aspect ratio (b/c)	2	–
Thickness-to-chord ratio (t/c)	0.5	–
Pitch-to-chord ratio (S/c)	0.85	–

As mentioned previously, the number of axial turbine stages is governed by the mechanical integrity of the turbine blades. Both rotor blade centrifugal and gas bending stresses were calculated for all possible mixture compositions. Unlike steam or gas turbines, centrifugal stress is not the dominant source of mechanical stress in CO_2 turbines. As seen in Fig. 18, gas bending stresses are greater by an order of magnitude.

In general, the tensile centrifugal stress is determined by the turbine's rotational speed and annulus area according to Eq. (27):

$$\sigma_{ct} = 2\pi K N^2 \rho_b A_{avg}/3600 \tag{27}$$

where the coefficient K depends on the taper of the blade and is set to 2/3 assuming a tapered blade [35], ρ_b is the density of the blade (appx. 8000 kg/m^3), and A_{avg} is the average annulus area between rotor inlet and outlet.

The rotational speed was fixed to a relatively moderate value of 3000 RPM to allow direct connection to a 50 Hz synchronous electric generator, without the need for a gearbox. On the other hand, the annulus area is narrower than that of gas turbines because of the low volumetric flow rate of the working fluid. Both of these factor reduce the significance of centrifugal stresses.

Gas bending stress may be expressed as a function of the fluid density, stage enthalpy drop, flow coefficient, and stage geometric

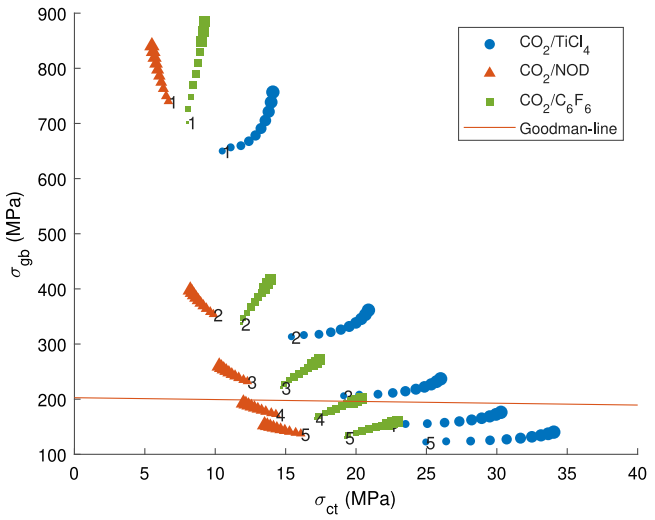

Fig. 18. Maximum allowable blade mechanical stresses based on number of turbine stages. The numbers denote the number of turbine stages corresponding to the plotted points and the point size is proportional to the dopant fraction.

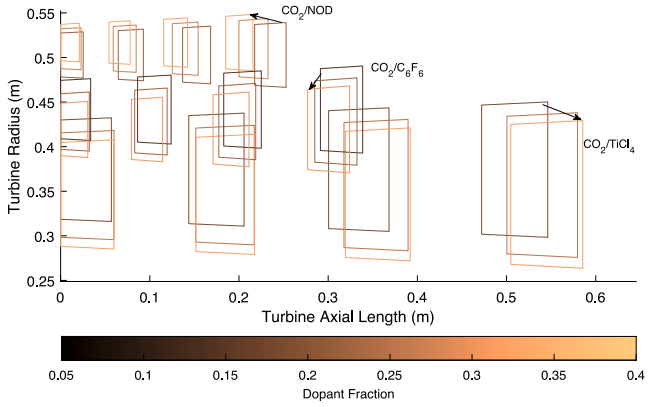

Fig. 19. Transformation of rotor blade profiles based on dopant molar fraction.

relations:

$$\sigma_{gb} = \left(\frac{4\pi\varphi N}{60}\right)\left(\frac{r_{s/c} r_{b/c}^{\,2}}{z}\right)\rho\Delta h \;\rightarrow\; \sigma_{gb} \propto \rho\Delta h \tag{28}$$

The flow coefficient (ϕ) and stage geometric relations ($r_{s/c}$, $r_{b/c}$) were chosen based on gas turbine best practices, thus are not the cause for the high stresses. The strong aerodynamic stresses are likely to be caused by the fluid's high density and the stage enthalpy drop. Since the density is imposed by optimal cycle conditions, the stress may otherwise be alleviated by increasing the number of stages to reduce the enthalpy drop per stage. As seen in Fig. 18, at least 4 stages are required to remain below the maximum design stress. The figure also shows that higher dopant fractions produce greater gas bending stresses. However, the difference between the stresses for all fractions reduces with increasing number of stages. One could argue that the number of stages is no longer affected by the blend fraction for axial turbine with three or more stages. The severity of aerodynamic stresses in sCO_2 turbines have been identified in previous publications [36–38].

Fig. 19 illustrates the meridional profiles of the turbine rotors for the range of blend fractions considered and may be studied to draw a comparison between two trends: (1) the different turbine geometries of the three dopants; (2) and the varying turbine geometries of the same mixture, but with changing dopant fractions.

For a fixed loading coefficient and rotational speed, the diameter of the turbine becomes a sole function of the enthalpy drop. Therefore,

Table 5
Comparison of design and performance parameters of 100 MWe pure sCO_2 and tCO_2 power plants operating with different mixtures.

Working fluid	CO_2	$CO_2/TiCl_4$	CO_2/NOD	CO_2/C_6F_6
Dopant molar fraction	0	0.174	0.264	0.167
Thermal efficiency (%)	41.7	49.5	42.3	46.5
Recuperator effectiveness (%)	98.5	95.9	98	93.1
Recuperator heat load (MW)	398	844	389	799
PHE inlet temperature (K)	762	823	687	819
PHE heat load (MW)	242	204	239	217
Turbine				
Mass flow rate (kg/s)	902	1393	738	1054
Exhaust volume flow rate (m^3/s)	7.03	6.88	5.11	5.31
Inlet temperature (K)	973	973	973	973
Outlet temperature (K)	817	869	817	877
Enthalpy drop (MJ/kg)	186	88.8	163	120
Mean diameter (m)	1.09	0.753	1.02	0.873
Axial length (m)	0.32	0.61	0.27	0.38

CO_2/NOD turbines, which experience higher enthalpy drops per stage, require wider turbines than CO_2/C_6F_6 or $CO_2/TiCl_4$. On the other hand, the blade height is influenced by the volume flow rate and enthalpy drop of the turbine in accordance with Eq. (29):

$$b \propto \dot{V}/\Delta h \tag{29}$$

As seen in Fig. 20, $CO_2/TiCl_4$ requires the longest blades, followed by CO_2/C_6F_6 and CO_2/NOD, which is explained by its higher volume flow rates and lower specific work. Moreover, the blade heights of $CO_2/TiCl_4$ and CO_2/C_6F_6 increase with blend fraction but decrease for CO_2/NOD blends.

Since the blade aspect ratio is fixed, the chord length becomes linearly proportional to the blade height. Therefore, the chord length increases with blade length, and the axial length of the turbine increases by consequence. Accordingly, in a transcritical cycle, one might expect the turbine to have a wider diameter and shorter length for mixtures that increase its specific work.

As previously noted, the expansion ratio increases with blend fraction for all mixtures. This is demonstrated in Fig. 21, which plots the normalised heights of the turbine rotor blades, where the change in blade height is proportional to the expansion ratio across the turbine. The change in blade height with each stage increases with blend fraction for all mixtures, suggesting that the turbine flare angle increases with blend fraction. However, CO_2/C_6F_6 exhibits the greatest increase.

A schematic of the *T-s* diagram and turbine flow paths meridional view corresponding to the optimal points are illustrated in Figs. 22 and 23. The cycle and turbine parameters corresponding to the compositions, pressure ratio, and recuperator effectiveness that yield optimal cycle efficiency are summarised in Table 5. Although there are notable differences between the four working fluids, they share comparably high mass-flow rates in the order of 1000 kg/s, and relatively low volumetric flow rates below 10 m^3/s. To put these number into perspective, the H-100 gas turbine manufactured by Mitsubishi has a similar capacity of around 100 MW, and exhausts about 300 kg/s of air at approximately 550 °C. Assuming ideal gas and ambient pressure conditions, this translates to 700 m^3/s. Therefore, the contrast between air and CO_2-based turbines' design space shows in both mass and volume flow rates.

Not only do blended CO_2 cycles outperform pure CO_2 in simple recuperated cycles, they also outperform pure CO_2 in recompression plants. Modelling of recompression cycle with similar boundary conditions, equipment efficiencies, 89% recompressor efficiency, and 0.79 split fraction yields an overall thermal efficiency of 43.4%. This comparison suggests that dopants like $TiCl_4$ and C_6F_6 achieve higher thermal efficiencies even in simpler cycle layouts.

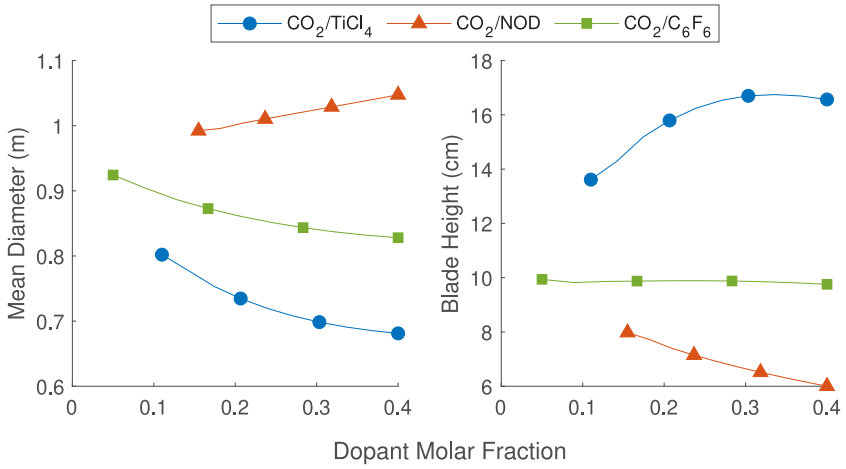

Fig. 20. Variation of mean diameter and rotor blade height at last stage with dopant molar fraction.

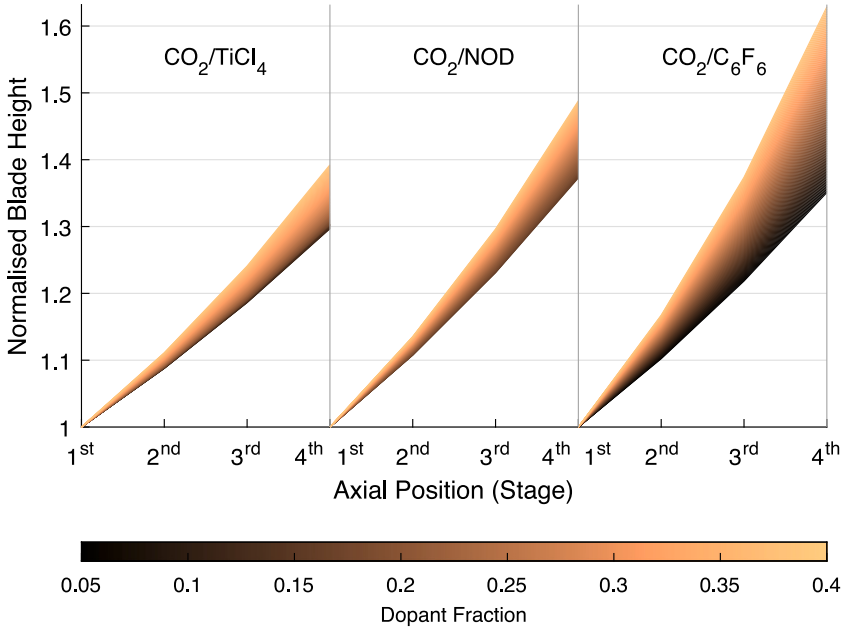

Fig. 21. Normalised stage-wise rotor blade height for the range of dopant molar fraction.

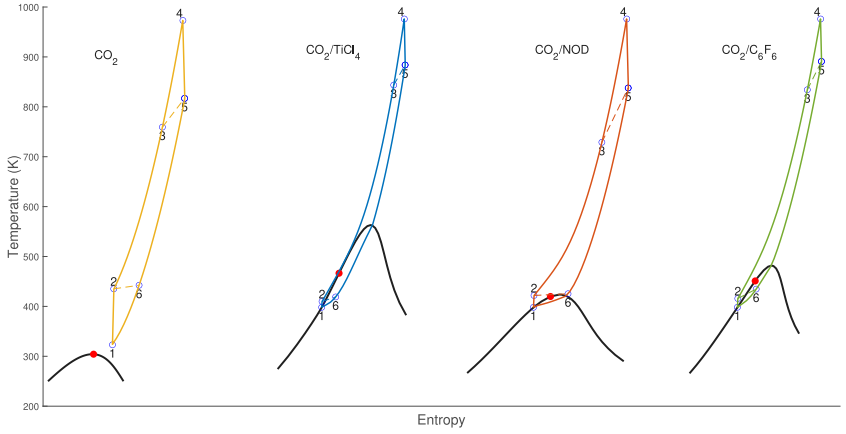

Fig. 22. Schematic of the *T-s* diagram for the dopant fraction and cycle conditions that yield optimal thermal efficiency. The critical point is indicated by a red dot.

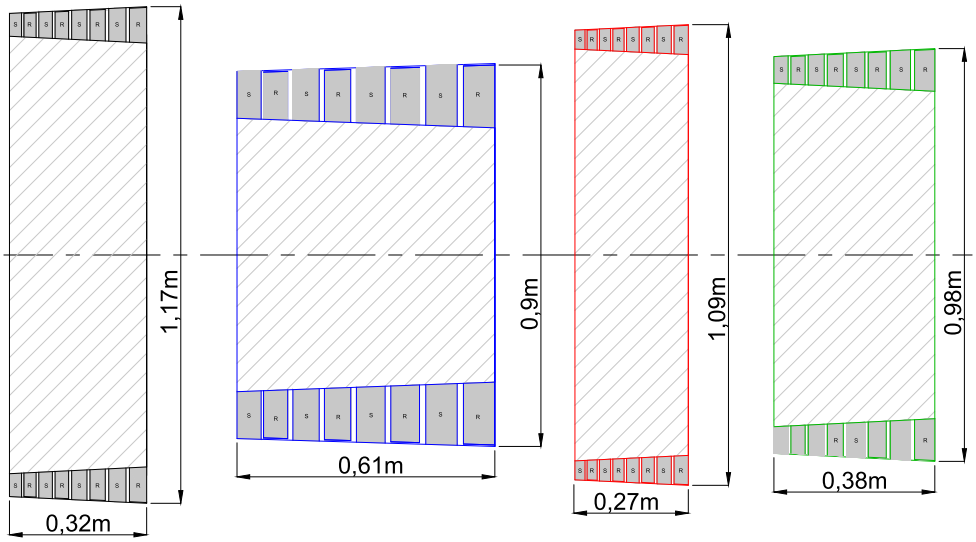

Fig. 23. Comparison of turbine flow paths meridional view corresponding to the design point that yields optimal thermal efficiency for pure CO_2 and CO_2-based mixtures. Left to right: Pure CO_2; $CO_2/TiCl_4$; CO_2/NOD; CO_2/C_6F_6.

4. Conclusion

The comparative analysis presented in this paper has investigated the effect of three dopants ($TiCl_4$, NOD, or C_6F_6) and their amounts on the optimal thermodynamic cycle conditions and the resulting turbine design for a 100 MW CSP power plant operating with sCO_2 blends. Increasing dopant molar fraction was found to increase the pressure ratio for all blends. The maximum achievable efficiencies were found to be 49.5%, 46.5%, and 42.3% for molar fractions of 0.21 of $CO_2/TiCl_4$, 0.32 of CO_2/NOD, and 0.17 of CO_2/C_6F_6. The adoption of molecularly complex dopants has been shown to alleviate the irreversibilities in the recuperator and enables condensing cycles to be realised with dry cooling. This could lead to higher thermal efficiencies compared to equivalent cycles operating with pure CO_2, which achieves an efficiency of 44.0%, but at the cost of possibly larger recuperators.

In terms of turbine design, the specific work was found to decrease with increasing fraction of $TiCl_4$ and C_6F_6, but increase with NOD. Moreover, the addition of any of the three dopants increases the pressure, temperature, and expansion ratios across the turbine; except for C_6F_6, which exhibits an almost constant temperature ratio. The fluid's density at turbine inlet increases with all dopants as well. Conversely, the speed of sound at turbine inlet decreases with all dopants, yet higher Mach numbers are expected in CO_2/C_6F_6 turbines.

By studying a 100 MWe power plant as an example, preliminary turbine sizing data was presented. This serves to investigate the sensitivity of the turbine design to the blend and molar fraction before moving onto a more detailed turbine design optimisation stage. Since heavier working fluids reduce the specific work, they increase the mass flow rate into the turbine, which in turn requires larger flow annuli. On the other hand, the turbine mean diameter is smaller for heavy working fluids. Therefore, assuming a fixed number of stages and the same design inputs, they require narrower but longer turbines compared to the lighter dopant (NOD).

Blade mechanical stresses were found to be dominated by gas bending stresses induced by aerodynamic forces. Modifying the CO_2 working fluid for condensing cycles in CSP applications necessitates dopants heavier than CO_2 to increase its critical temperature. Increasing the density of the working fluid will further exacerbate the blade mechanical stresses. Dedicated optimisation studies of turbine design should be undertaken to lower the aerodynamic stresses by adding more blades or increasing blade chord or thickness. Ultimately, a compromise between turbine size, mechanical strength, and aerodynamic efficiency can be made.

The topic of power cycles operating with CO2-based mixtures still requires further study. An informed decision of the most suitable dopant must account for techno-economic considerations. The effect of the relatively high temperature glides in $CO_2/TiCl_4$ and CO_2/C_6F_6 recuperators on heat exchanger design remains to be examined. Moreover, additional equipment may be needed to address the fractionation of $CO_2/TiCl_4$ and CO_2/C_6F_6 during heat rejection, which may increase the plant size and cost. Another, deciding factor pertaining to fluid selection is off-design analysis, which is increasingly important in the design of CSP plants which are subject to daily and seasonal variations.

CRediT authorship contribution statement

O.A. Aqel: Conceptualization, Methodology, Software, Formal analysis, Investigation, Writing - original draft, Visualization. **M.T. White:** Conceptualization, Methodology, Software, Investigation, Writing - review & editing, Supervision. **M.A. Khader:** Software, Writing - review & editing. **A.I. Sayma:** Writing - review & editing, Supervision, Funding acquisition.

Declaration of competing interest

The authors declare that they have no known competing financial interests or personal relationships that could have appeared to influence the work reported in this paper.

Acknowledgement

This project has received funding from the European Union's Horizon 2020 research and innovation programme under grant agreement No. 814985.

References

[1] G. Musgrove, S. Wright, Introduction and background, in: Fundamentals and Applications of Supercritical Carbon Dioxide (SCO2) Based Power Cycles, Elsevier, 2017, pp. 1–22, http://dx.doi.org/10.1016/B978-0-08-100804-1.00001-3, URL https://linkinghub.elsevier.com/retrieve/pii/B9780081008041000013.

[2] S. Polimeni, M. Binotti, L. Moretti, G. Manzolini, Comparison of sodium and KCl-MgCl2 as heat transfer fluids in CSP solar tower with sCO2 power cycles, Sol. Energy 162 (2018) 510–524, http://dx.doi.org/10.1016/j.solener.2018.01.046.

[3] K. Wang, Y.L. He, H.H. Zhu, Integration between supercritical CO2 brayton cycles and molten salt solar power towers: A review and a comprehensive comparison of different cycle layouts, Appl. Energy 195 (2017) 819–836, http://dx.doi.org/10.1016/j.apenergy.2017.03.099.
[4] T. Neises, C. Turchi, A comparison of supercritical carbon dioxide power cycle configurations with an emphasis on CSP applications, in: Energy Procedia, Vol. 49, Elsevier Ltd, 2014, pp. 1187–1196, http://dx.doi.org/10.1016/j.egypro.2014.03.128.
[5] M. Atif, F.A. Al-Sulaiman, Energy and exergy analyses of solar tower power plant driven supercritical carbon dioxide recompression cycles for six different locations, in: Renewable and Sustainable Energy Reviews, Vol. 68, Elsevier Ltd, 2017, pp. 153–167, http://dx.doi.org/10.1016/j.rser.2016.09.122.
[6] M. Cerio Vera, S-CO2 for Efficient Power Generation with Energy Storage, Tech. Rep., 2015.
[7] J.D. Osorio, R. Hovsapian, J.C. Ordonez, Effect of multi-tank thermal energy storage, recuperator effectiveness, and solar receiver conductance on the performance of a concentrated solar supercritical CO 2 -based power plant operating under different seasonal conditions, Energy 115 (2016) 353–368, http://dx.doi.org/10.1016/j.energy.2016.08.074.
[8] R. Privat, J.N. Jaubert, Classification of global fluid-phase equilibrium behaviors in binary systems, Chem. Eng. Res. Des. 91 (10) (2013) 1807–1839, http://dx.doi.org/10.1016/j.cherd.2013.06.026.
[9] T.G. Lewis, T.M. Conboy, S.A. Wright, Supercritical CO2 Mixture Behavior for Advanced Power Cycles and Applications, Tech. Rep, 2011.
[10] R. Valencia-Chapi, L. Coco-Enríquez, J. Muñoz-Antón, Supercritical CO2 mixtures for advanced brayton power cycles in line-focusing solar power plants, Appl. Sci. (Switzerland) 10 (1) (2020) http://dx.doi.org/10.3390/app10010055.
[11] W.S. Jeong, Y.H. Jeong, Performance of supercritical brayton cycle using CO2-based binary mixture at varying critical points for SFR applications, Nucl. Eng. Des. 262 (2013) 12–20, http://dx.doi.org/10.1016/j.nucengdes.2013.04.006.
[12] C.M. Invernizzi, T. Van Der Stelt, Supercritical and real gas brayton cycles operating with mixtures of carbon dioxide and hydrocarbons, Proc. Inst. Mech. Eng. A: J. Power Energy 226 (5) (2012) 682–693, http://dx.doi.org/10.1177/0957650912444689.
[13] J. Xia, J. Wang, G. Zhang, J. Lou, P. Zhao, Y. Dai, Thermo-economic analysis and comparative study of transcritical power cycles using CO2-based mixtures as working fluids, Appl. Therm. Eng. 144 (2018) 31–44, http://dx.doi.org/10.1016/j.applthermaleng.2018.08.012.
[14] G. Manzolini, M. Binotti, D. Bonalumi, C. Invernizzi, P. Iora, CO 2 mixtures as innovative working fluid in power cycles applied to solar plants. Techno-economic assessment, Sol. Energy 181 (June 2018) (2019) 530–544, http://dx.doi.org/10.1016/j.solener.2019.01.015.
[15] M. Binotti, C.M. Invernizzi, P. Iora, G. Manzolini, Dinitrogen tetroxide and carbon dioxide mixtures as working fluids in solar tower plants, Sol. Energy (2019) 203–213, http://dx.doi.org/10.1016/j.solener.2019.01.079.
[16] F. Crespi, G. Gavagnin, D. Sánchez, G.S. Martínez, Supercritical carbon dioxide cycles for power generation: A review, 2017, http://dx.doi.org/10.1016/j.apenergy.2017.02.048.
[17] SCARABEUS, SCARABEUS Project, 2019, URL https://www.scarabeusproject.eu/.
[18] V. Dostal, M.J. Driscoll, P. Hejzlar, A supercritical carbon dioxide cycle for next generation nuclear reactors, 2004, URL http://web.mit.edu/canes/.
[19] D. Novales, A. Erkoreka, V. De la Peña, B. Herrazti, Sensitivity analysis of supercritical CO 2 power cycle energy and exergy efficiencies regarding cycle component efficiencies for concentrating solar power, Energy Convers. Manage. 182 (September 2018) (2019) 430–450, http://dx.doi.org/10.1016/j.enconman.2018.12.016, URL https://doi.org/10.1016/j.enconman.2018.12.016.
[20] T.C. Allison, J. Moore, R. Pelton, J. Wilkes, B. Ertas, Turbomachinery, in: Fundamentals and Applications of Supercritical Carbon Dioxide (SCO2) Based Power Cycles, Elsevier Inc., 2017, pp. 147–215, http://dx.doi.org/10.1016/B978-0-08-100804-1.00007-4.
[21] J.J. Sienicki, A. Moisseytsev, R.L. Fuller, S.A. Wright, P.S. Pickard, Scale dependencies of supercritical carbon dioxide brayton cycle technologies and the optimal size for a next-step supercritical CO 2 cycle demonstration, 2011.
[22] C.H.S.L. Dixon, Fluid Mechanics and Thermodynamics of Turbomachinery, seventh ed., Butterworth-Heinemann, 2014, p. 556.
[23] H.I.H. Saravanamuttoo, G.F.C. Rogers, H. Cohen, P.V. Straznicky, A.C. Nix, H. Saravanamuttoo, P.V. Straznicky, Gas Turbine Theory, Seventh ed., Pearson Education Limited, 2017, pp. 100–123, URL www.pearson.com/uk.
[24] S.I. Salah, M.A. Khader, M.T. White, A.I. Sayma, Mean-line design of a supercritical CO 2 micro axial turbine, Appl. Sci. (Switzerland) (2020) 1–20, http://dx.doi.org/10.3390/app10155069.
[25] PCC Energy Group, Inconel® Alloy 740H: A Superalloy Specifically Designed for Advanced Ultra Supercritical Power Generation, Tech. Rep., 2014, URL http://www.specialmetals.com/files/PCCEG740HWhitePaper.pdf.
[26] ProSim, Simulis thermodynamics, 2019, URL http://www.prosim.net/en/software-simulis-thermodynamics-mixture-properties-and-fluid-phase-equilibria-calculations-3.php.
[27] D. Bonalumi, S. Lasala, E. Macchi, CO2-TiCl4 working fluid for high-temperature heat source power cycles and solar application, Renew. Energy (2018) http://dx.doi.org/10.1016/j.renene.2018.10.018.
[28] S. Hajipour, M.A. Satyro, M.W. Foley, Uncertainty analysis applied to thermodynamic models and process design-2. Binary mixtures, Fluid Phase Equilib. 364 (2014) 15–30, http://dx.doi.org/10.1016/j.fluid.2013.12.004.
[29] A.M. Dias, H. Carrier, J.L. Daridon, J.C. Pàmies, L.F. Vega, J.A. Coutinho, I.M. Marrucho, Vapor - liquid equilibrium of carbon dioxide - perfluoroalkane mixtures: Experimental data and SAFT modeling, Ind. Eng. Chem. Res. 45 (7) (2006) 2341–2350, http://dx.doi.org/10.1021/ie051017z.
[30] M. Petrollese, D. Cocco, A multi-scenario approach for a robust design of solar-based orc systems, Renew. Energy 161 (2020) 1184–1194, http://dx.doi.org/10.1016/j.renene.2020.07.120.
[31] K. Braimakis, S. Karellas, Energetic optimization of regenerative organic rankine cycle (ORC) configurations, Energy Convers. Manage. 159 (January) (2018) 353–370, http://dx.doi.org/10.1016/j.enconman.2017.12.093.
[32] C. Schifflechner, F. Dawo, S. Eyerer, C. Wieland, H. Spliethoff, Thermodynamic comparison of direct supercritical CO2 and indirect brine-ORC concepts for geothermal combined heat and power generation, Renew. Energy 161 (2020) 1292–1302, http://dx.doi.org/10.1016/j.renene.2020.07.044.
[33] F. Wei, G. Senchuang, H. Zhonghe, Economic analysis of organic rankine cycle (ORC) and organic rankine cycle with internal heat exchanger (IORC) based on industrial waste heat source constraint, Energy Procedia 158 (2019) 2403–2408, http://dx.doi.org/10.1016/j.egypro.2019.01.291.
[34] S. Lasala, R. Privat, J.-N. Jaubert, Inert and reactive working fluids for closed power cycles: Present knowledge, applications and open researches, Org. Rank. Cycle Technol Heat Recovery (2018) 3–18, http://dx.doi.org/10.5772/intechopen.79290.
[35] H. Moustapha, M.F. Zelesky, C.N. Baines, D. Japikse, Axial and Radial Turbines, Concepts ETI, Inc., 2003.
[36] H. Zhang, H. Zhao, Q. Deng, Z. Feng, Aerothermodynamic design and numerical investigation of supercritical carbon dioxide turbine, in: Proceedings of the ASME Turbo Expo, Vol. 9, 2015, pp. 1–9, http://dx.doi.org/10.1115/GT2015-42619.
[37] S. Co, Gt2014-25385 turbomachinery flowpath design and performance analysis for, 2014, pp. 1–8.
[38] Y. Wang, G. Guenette, P. Hejzlar, M. Driscoll, Compressor design for the supercritical CO 2 brayton cycle, Collection of Technical Papers - 2nd International Energy Conversion Engineering Conference, Vol. 3(August), 2004, pp. 1599–1611, http://dx.doi.org/10.2514/6.2004-5722.